M. Greiner
Associate Professor,
Assoc. Mem. ASME
e-mail: greiner@unr.edu

R. J. Faulkner
Research Assistant

V. T. Van
Research Assistant

Mechanical Engineering Department,
University of Nevada,
Reno, NV 89557

H. M. Tufo
Department of Computer Science,
University of Chicago,
Chicago, IL 60637

P. F. Fischer
Mathematics and Computer Science Division,
Argonne National Laboratory,
Argonne, IL 60439

Simulations of Three-Dimensional Flow and Augmented Heat Transfer in a Symmetrically Grooved Channel

Navier-Stokes simulations of three-dimensional flow and augmented convection in a channel with symmetric, transverse grooves on two opposite walls were performed for $180 \leqslant Re \leqslant 1600$ *using the spectral element technique. A series of flow transitions was observed as the Reynolds number was increased, from steady two-dimensional flow, to traveling two and three-dimensional wave structures, and finally to three-dimensional mixing. Three-dimensional simulations exhibited good agreement with local and spatially averaged Nusselt number and friction factor measurements over the range* $800 \leqslant Re \leqslant 1600$. [S0022-1481(00)00904-X]

Keywords: Augmentation, Computational, Forced Convection, Heat Transfer, Unsteady

Introduction

Engineering devices frequently employ enhanced heat transfer surfaces ([1]). Fins are typically used to extend surface areas and offset strips are often employed to promote thin boundary layers. In recent years a number of configurations that excite flow instabilities have been considered. Transversely grooved channels ([2–4]), passages with eddy promoters ([5,6]), and communicating channels ([7]) all contain fairly large features whose size is roughly half the channel wall-to-wall spacing. These features promote inflections in the passage velocity profile. Kelvin-Helmholtz instabilities of these inflected profiles project energy onto normally damped Tollmien-Schlichting waves, resulting in two-dimensional traveling waves at moderately low Reynolds numbers.

The current authors have presented a series of articles on rectangular cross-section passages with a contiguous set of transverse, V-shaped grooves cut into one wall. Experimental flow visualizations show that the grooves excite two-dimensional waves at Reynolds numbers as low as $Re=350$, followed by an early transition to three-dimensional mixing ([8]). Transport measurements using air show that both the Nusselt number and friction factor are greater than the corresponding values for a flat channel with the same minimum wall to wall spacing ([9]). A significant result is that fully developed heat transfer is enhanced relative to laminar flat channel flow by factors as large as 4.6 at equal Reynolds numbers and by a factor of 3.5 at equal pumping powers.

Navier-Stokes simulations of flow and heat transfer in the same grooved channel geometry were performed using the spectral element method ([10]). These simulations employed a computational domain that represents one periodicity cell of the grooved passage. A constant body force was applied uniformly to the fluid. This forcing is equivalent to driving the flow with a constant pressure drop across the computational domain. The unsteady flow field occasionally forces slow moving fluid from the groove into the fast external channel causing the volume flow rate to be very unsteady. At $Re=2000$ the amplitude of the flow rate unsteadiness was 30 percent of the mean value. The friction factor and Nusselt number versus Reynolds number relationships predicted by these simulations were within 20 percent of the earlier experiments. Moreover, two-dimensional simulations were shown to be incapable of capturing the transport processes in this channel for Reynolds numbers greater than $Re=570$.

The experiments by Greiner et al. [9] did not measure the time variations of the flow rate passing through the passage. However, two phenomena suggest that the experimental flow rate unsteadiness was smaller than the numerically predicted level. The first is that the experimental passage had 46 grooves and it is not likely that the flow in each groove was synchronized. Secondly, the experimental apparatus contained long flat sections whose inertia tends to reduce flow rate unsteadiness. Investigations of resonant heat transfer augmentation in grooved channels indicate that imposing unsteady flow rates at subcritical (normally steady) Reynolds numbers has the potential to more than double the heat transfer level compared to a constant flow rate ([3,11]). The good agreement between the numerical and experimental results suggests that flow rate unsteadiness has less effect on heat transfer at supercritical (normally unsteady) Reynolds numbers, but this effect has not been investigated.

Finally, all of our earlier heat transfer results employed a constant temperature on the grooved boundary and a uniform heat flux from the opposite flat surface. The heat transfer coefficients therefore quantify transport augmentation *from one surface to the other* and not the heat transfer to the bulk fluid.

In the current work, we consider a symmetrically grooved channel (with grooves on *both* surfaces) with constant temperature boundary conditions. The double-grooved geometry is more easily implemented in heat exchangers than the earlier configuration. The constant temperature wall conditions quantify the heat transfer from the passage to the fluid, and hence are more realistic for assessing the applicability of grooved channels to heat exchanger applications. Simulations are performed for both constant body

Contributed by the Heat Transfer Division for publication in the JOURNAL OF HEAT TRANSFER. Manuscript received by the Heat Transfer Division, Aug. 23, 1999; revision received, May 25, 2000. Associate Technical Editor: R. W. Douglass.

force and constant flow rate conditions to assess the effect of unsteady flow rate on transport at supercritical Reynolds numbers.

This work was performed in parallel with an experimental study ([12]). That work used a holographic interferometer to measure local heat transfer in the fully developed region of a passage with seven symmetric grooves. That measurement system was better suited for evaluating the fluid centerline temperature than it was for measuring bulk values, and hence the measured heat transfer coefficients are based on the centerline temperature. Analogous centerline Nusselt number and friction factor results are determined in the current numerical work and are directly compared to the experimental data.

Numerical Method

Computational Domain. Figure 1 shows the three-dimensional domain and spectral element mesh employed in this work. The upper and lower V-shaped boundaries are solid walls, and the fluid flows from left to right. The groove depth $a = 0.012$ m, groove length $b = 0.024$ m, and minimum wall-to-wall spacing $H = 0.01$ m are identical to the dimensions used in the companion experimental study ([12]). This domain is the same as our earlier studies of a channel with one grooved wall ([8–10]) except grooves are now placed on both the top and bottom surfaces. The groove dimensions were chosen to be compatible with the most slowly decaying Tollmien-Schlichting waves of the external channel flow.

Periodicity is imposed on the inflow and outflow boundaries at $x = 0$ and b. As a result these simulations model flows that are periodic from groove to groove. Periodicity is also imposed on the boundaries at $z = 0$ and W, where $W = 0.02$ m. The computational grid consists of four levels in the z-direction, each containing 160 hexahedral spectral elements ([13,14]), for a total of $K = 640$ elements. The mesh is more refined near the peaks of the grooves than in the rest of the domain. Within each element, the solution, data and geometric mapping are expressed as tensor-product polynomials of degree N in each spatial direction, corresponding to a total grid point count of roughly KN^3. Numerical convergence is achieved by increasing the spectral order N. Simulations in this work are performed with $N = 7$ and 9.

A shortcoming of the x and z-direction periodicity conditions is that they only admit modal wavelengths such that an integer number of waves exactly span the domain. That is x-direction and z-direction wavelengths equal to b/m and W/n, respectively, where m and n are integers. This limitation is most severe when the dominant flow field wavelengths are larger than or roughly the same as the domain dimensions. We will see that the eddy sizes generally decrease with increasing Reynolds number. As a result it is possible that the current simulations overpredict the Reynolds number where two and three-dimensional modes first appear. However, the periodicity limitation is less important to the prediction of transport quantities at higher Reynolds numbers.

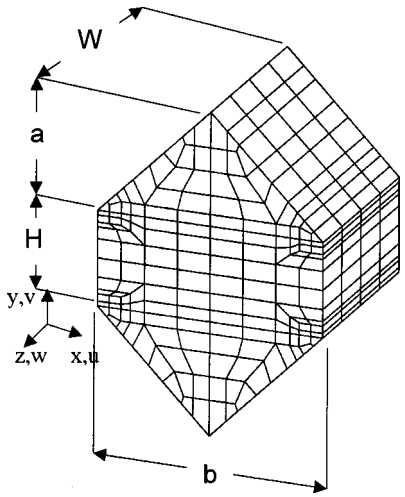

Fig. 1 Spectral element mesh

Two variations of the mesh are used to demonstrate grid independence. In mesh B, six z-levels are used instead of four to determine if a more refined grid affects the results. Mesh C has width $W = 0.03$ m and six z-levels. It is used to determine if a wider domain affects the results. Grid independence is also demonstrated by performing simulations with different spectral orders, N. Finally, two-dimensional simulations are performed using a planar grid equivalent to the face of the domain in Fig. 1.

Flow Field. The present simulations use a fractional step (or time splitting) approach ([15,16]). In this technique, the coupled momentum equations are advanced by first computing the convection term, followed by the projection of the velocity onto a divergence-free space, and finally a viscous update which incorporates the velocity boundary conditions.

The flow is driven from left to right by a uniform body force per unit mass f_x. This forcing is equivalent to a specified pressure drop across the domain, i.e., $f_x = \Delta p/(b\rho)$. At each time step, the velocity is integrated over the domain to determine the average speed through the minimum channel cross section, $U = (\int_\Omega u dV)/(bWH)$. This speed is used to calculate the Reynolds number $\mathrm{Re} = UD_h/\nu$, where $D_h = 2H$ is the hydraulic diameter of a flat passage with the same minimum wall to wall spacing as the grooved channel.

Simulations are performed beginning with an initial condition (zero velocity or a lower Reynolds number solution) and are run until ''steady state'' is observed for roughly one second of flow time. We will see that steady state at low Reynolds numbers is time-independent. However, as the Reynolds number increases, the flow field exhibits first time-periodic behavior and then random variations about a ''constant'' mean value.

Calculations are performed for both constant f_x (specified ''*cfx*'') and for constant flow rate (*cfr*) forcing conditions. For constant f_x calculations, the Reynolds number varies with time. For constant flow rate simulations the value of f_x is varied at each time step so that the Reynolds number remains constant ([16]).

For constant f_x simulations, the time-averaged speed U_a is computed after the flow field reaches steady state by averaging backwards from the final time over successively longer intervals until the result converged. This speed is used in the time-averaged Reynolds number $\mathrm{Re}_a = U_a D_h/\nu$ and time-averaged Fanning friction factor $f = (f_x D_h)/(2U_a^2)$. For constant flow rate simulations, the time average value of f_x is used in the calculation of the Fanning factor.

Constant Temperature Boundary Conditions. The solution technique for computing the fully developed temperature field for constant temperature boundary conditions follows the analysis of Patankar et al. [17]. The energy equation, and associated initial and boundary conditions are

$$\frac{\partial T}{\partial t} + \vec{U}\cdot\nabla T = \alpha\cdot\nabla^2 T \tag{1a}$$

$$T(x,y,z,t=0) = T_{\mathrm{init}}(x,y,z) \tag{1b}$$

$$T(x,y,z,t) = 0 \quad \text{on the walls} \tag{1c}$$

$$T(x=b,y,z,t) = e^{-cb}T(x=0,y,z,t). \tag{1d}$$

Equation (1*d*) corresponds to the fully developed and periodic condition where the temperature profile is self-similar from one cell to the next, i.e., $T(x+b,y,z,t) = e^{-cb}T(x,y,z,t)$ for all (x, y, z, t). The constant c is unknown and is a parameter to be deter-

mined as part of the computation. The fact that each cell independently satisfies the homogeneous Eq. (1) and that we are considering fully developed solutions that are independent of T_{init} implies that the solution to (1) for each cell would yield the same value of c. Hence, c cannot be a function of x. Moreover, it is readily demonstrated from energy arguments that under fully developed conditions c cannot be a function of time even when the flow is itself unsteady.

Any function satisfying the above self-similar condition has the unique decomposition $T(x,y,z,t)=e^{-cx}\theta(x,y,z,t)$ where $\theta(x+b,y,z,t)=\theta(x,y,z,t)$ is a periodic function. Thus, the computation of T is reduced to the computation of a periodic function θ, and the constant c. Substituting this decomposition into Eq. (1) yields

$$\frac{\partial\theta}{\partial t}+\vec{U}\cdot\nabla\theta-\alpha\cdot\nabla^2\theta=(\alpha\cdot c^2+uc)\theta-2\alpha\cdot c\frac{\partial\theta}{\partial x} \tag{2a}$$

$$\theta(x,y,z,t=0)=\theta_{\text{init}}(x,y,z) \tag{2b}$$

$$\theta(x,y,z,t)=0 \quad \text{on the walls} \tag{2c}$$

$$\theta(x=b,y,z,t)=\theta(x=0,y,z,t). \tag{2d}$$

Since the fully developed solution is independent of the initial condition we may arbitrarily set $\theta_{\text{init}}=1$. Equation (2a) is solved using a semi-implicit time-stepping procedure similar to that for our Navier-Stokes solver. The diffusive terms are treated implicitly while the convective terms are treated explicitly. In addition, all terms on the right of Eq. (2a) are treated explicitly using the latest available value for c.

In the steady-state case ($\partial/\partial t=0$), Eq. (2) constitutes an eigenproblem for the eigenpair (c,θ). The constant c corresponds to the decay rate of the mean temperature in the x-direction. As such, a larger value of c implies more rapid decay and more effective heat transfer. In the convection-dominated limit where the Peclet number $U_a b/\alpha$ is large, Eq. (2a) becomes a linear eignvalue problem. In this case standard iterative methods for computing the lowest value of c (corresponding to the most slowly decaying mode in x) can be used even when the nonlinear (c^2) term in Eq. (2a) is not identically zero. We find that this method accurately computes the decay rate and Nusselt numbers for steady flows in square and round ducts ([18]).

For steady periodic flows with period τ, the temperature is periodic in time, implying $T(x,y,z,t+\tau)=T(x,y,z,t)$. Since c is independent of time, this implies that $\theta(x,y,z,t+\tau)=\theta(x,y,z,t)$. If the value of c is not chosen correctly, this condition will not be satisfied. Unfortunately, τ is not known a priori but is a result of the hydrodynamic part of the calculation. A robust approach to compute c and θ is obtained by multiplying Eq. (2a) by θ, integrating over a single cell Ω, and simplifying to yield

$$\frac{1}{2}\frac{d}{dt}\int_\Omega\theta^2 dV=\int_\Omega[(\alpha c^2+uc)\theta^2-\alpha\nabla\theta\cdot\nabla\theta]dV. \tag{3}$$

While we do not expect the time derivative of the average temperature (represented by the left-hand side of Eq. (3)) to be identically zero, it will in general be less than the time derivative of θ at any one point in the domain. Moreover, if we integrate the right-hand side of Eq. (3) from time t to $t+\tau$, the resultant quantity must be zero due to the temporal periodicity.

This suggests a two-tier strategy for computing c in the unsteady case. Initially, we determine c such that the right-hand side of Eq. 3 is identically zero at each time step. This will permit a relatively coarse but quick determination of c and θ. Subsequently, once τ is well established, we use this value of c to advance θ for one or more periods, and monitor the decay or growth of $\int\theta^2 dV$. At the end of each trial period, we adjust c until convergence is attained.

The bulk fluid temperature in the domain $T_b=\int_\Omega uTdV/\int_\Omega udV$ and total heat transfer $q=\int_s(k\nabla T\hat{n})ds$ (where s includes both wall surfaces) are calculated at each time step. The time-dependent bulk and center-point Nusselt numbers are calculated using the expressions $\text{Nu}_b(t)=qD_h/kT_bA_p$ and $\text{Nu}_c(t)=qD_h/kT_cA_p$, respectively, where T_c is the center point fluid temperature at location $(x,y,z)=(b/2,H/2,W/2)$, and A_p is the total projected area of the surfaces $A_p=2Wb$. The time-average bulk and center-point Nusselt numbers $\text{Nu}_{c,a}$ and $\text{Nu}_{b,a}$, respectively, are calculated after transients decay and the time-dependent parameters reach steady state (exhibit constant window averaged values) for roughly one second. Then the time averages are calculated by averaging backwards from the final time over successively longer intervals until the results converge. Roughly 0.4 seconds of data are required at $\text{Re}_a=1630$ for an accurate time average.

The three-dimensional simulations are performed in parallel, using 64-bit arithmetic, on 128 i860 processors on the Intel Paragon at Caltech ([19,20]). The two-dimensional simulations are performed on 32 processors. A typical three-dimensional simulation requires 15 seconds per time step ($\Delta t=0.0002$ sec) for a spectral order of $N=7$. This results in about 21 hours of computer time to calculate one second of real flow time. Some Reynolds numbers can require as much as ten seconds of flow time to reach steady-state conditions.

Results

Velocity and Temperature Fields. This section describes spatial and temporal variations of the flow and temperature fields for a range of forcing levels, $f_x=0.2$ to 12.5 N/kg. All the results in this section are for constant f_x (*cfx*) simulations. Results for constant flow rate (*cfr*) are presented in the next section. Figures 2(*a*) and 2(*b*) show streamlines from two-dimensional simulations at $f_x=0.2$ and 0.5 N/kg after steady-state conditions have been reached. For $f_x=0.2$ N/kg the flow field is time-independent. The grooves are filled with slowly turning vortices and fluid in the

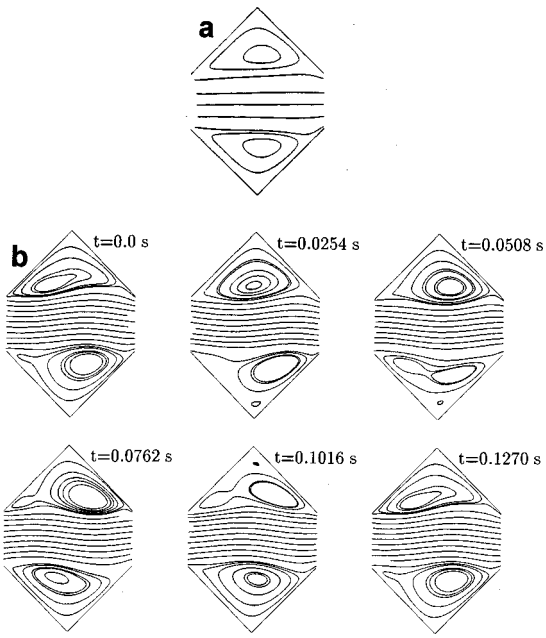

Fig. 2 Streamlines from two-dimensional simulations; (*a*) $f_x=0.2$ N/kg ($\text{Re}_a=180$), (*b*) $f_x=0.5$ N/kg ($\text{Re}_a=380$)

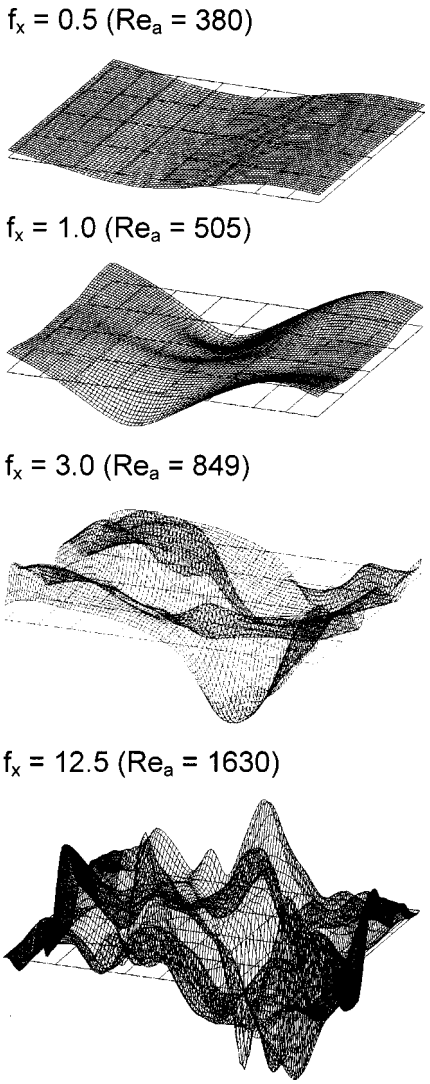

Fig. 3 Isometric views of *v*-velocity on the plane $y=H/2$

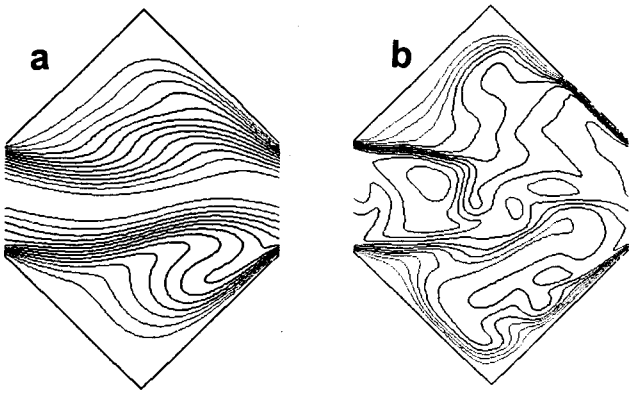

Fig. 5 Instantaneous isotherms at $z=0$; (*a*) $f_x=0.5$ N/kg ($Re_a=380$), (*b*) $f_x=3.0$ N/kg ($Re_a=849$)

open channel flows parallel to the *x*-direction. Integration of the velocity shows that the Reynolds number at this forcing level is $Re_a=180$.

Figure 2(*b*) shows streamlines at six equally spaced times for $f_x=0.5$ N/kg, corresponding to a time-averaged Reynolds number of $Re_a=380$. This flow exhibits a traveling wave structure with a wavelength equal to the channel periodicity length. We note that while this is the maximum wavelength that this computational domain can accommodate, the wavelength in a long grooved channel may actually be different. Moreover, the flow field repeats itself after a period of 0.1270 sec. The wave structure causes fluid to be alternately ejected from the top and bottom grooves. Similar traveling waves are observed in a single-grooved-wall channel at $Re=350$ ([8,10]).

Velocity data from two-dimensional simulation at $f_x=0.5$ N/kg were used as initial conditions for a three-dimensional simulation with the same forcing level. Figure 3 shows isometric views of the *y*-component of velocity (v) at the midplane $y=H/2$ at four different forcing levels, $f_x=0.5$, 1.0, 3.0, and 12.5 N/kg, corresponding to $Re_a=380$, 505, 849, and 1630, respectively. These surfaces are typical snapshots in time after steady-state conditions are reached. The velocity scale for each of these surfaces is the same.

The surface for $f_x=0.5$ N/kg shows that this flow field exhibits one wave in the *x*-direction and almost no variation in the *z*-direction. At $f_x=1.0$ N/kg the flow exhibits significant but regular variations in the *z*-direction. The variation in both the *x* and *z*-direction are much less regular at $f_x=3.0$ and 12.5 N/kg. The footprints of the peaks and valleys of these surfaces characterize the eddy length scales. We see that as the fluid forcing level and Reynolds number increase the flow structures become increasing irregular and their characteristic lengths decrease.

Figure 4 is a plot of the Reynolds number versus time for f_x

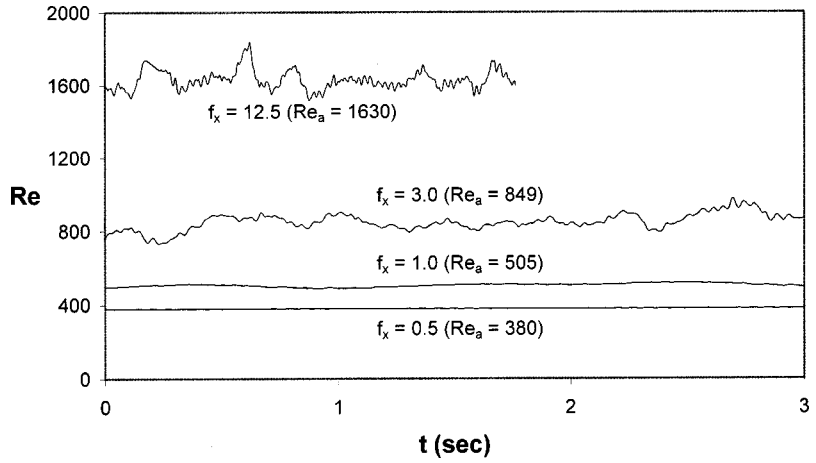

Fig. 4 Reynolds number versus time

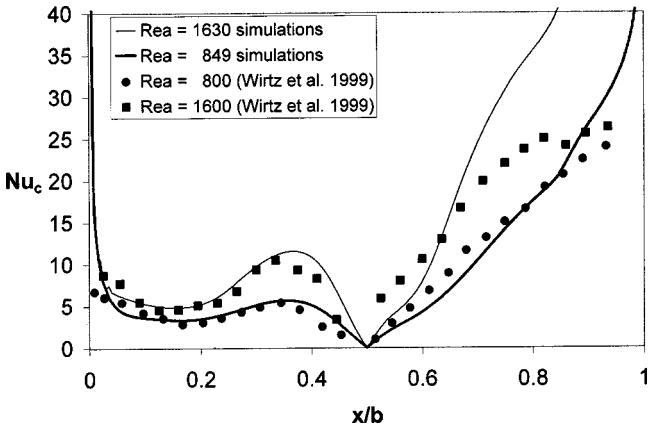

Fig. 6 Local center point Nusselt number versus location

=0.5, 1.0, 3.0, and 12.5 N/kg. These results are from three-dimensional simulations. Close examination of the $f_x=0.5$ N/kg data shows that the Reynolds number actually exhibits small oscillations with time. The period of this unsteadiness is 0.0635 sec, and its amplitude is only 0.14 percent of the mean value. These flow rate oscillations are caused by the periodic ejection of slow moving fluid from the grooves. The period of the Reynolds number oscillation is half the flow-field period since there are two fluid ejection events (from the top and bottom grooves) during each cycle. The Reynolds number versus time behavior from the three-dimensional simulation is essentially identical to that from two-dimensional calculations. This indicates that the small amount of three-dimensional behavior observed in Fig. 3 for $f_x=0.5$ N/kg does not significantly affect the flow rate.

The time-dependent Reynolds number for $f_x=1.0$ N/kg varies gently about a ''constant'' mean value of $\mathrm{Re}_a=505$. We note that *two*-dimensional simulations at this forcing level give a significantly greater time average Reynolds number of $\mathrm{Re}_a=640$. The lower flow rate predicted by three-dimensional simulations indicates that the structure exhibited in Fig. 3 for $f_x=1.0$ N/kg results in significantly higher levels of drag than two-dimensional waves.

As f_x increases to 3.0 and 12.5 N/kg ($\mathrm{Re}_a=849$ and 1630, respectively), the traces exhibit larger variations about their mean values and wider ranges of unsteady frequencies. The time step at $f_x=12.5$ N/kg is very small and so only 1.7 seconds of steady-state data was calculated at that forcing level.

Figures 5(*a*) and 5(*b*) show isotherms on planes of constant *z*-coordinate at $f_x=0.5$ and 3.0 N/kg ($\mathrm{Re}_a=380$ and 849). These snapshots are taken after steady-state conditions are reached. For $f_x=0.5$ N/kg, the isotherms in the outer channel exhibit a wave structure, and the effect of the vortices in transporting fluid within the grooves is evident. Snapshots at subsequent times show that this wave travels in the positive *x*-direction. Views at different *z*-locations are essentially identical, in agreement with the very small velocity variations observed in Fig. 3 for $\mathrm{Re}_a=380$.

For $f_x=1.0$ N/kg (not shown) the isotherms also exhibit smooth wave motion, similar to the pattern in Fig. 5(*a*). However, plots at different *z*-locations are not in phase. The isotherms for $f_x=3.0$ N/kg show that the temperature field is more irregular than it is at lower Reynolds numbers. Moreover, isotherms at different *z*-locations are substantially different from Fig. 5(*b*).

In Fig. 5 closely spaced isotherms near the walls indicate thin boundary layers. For both $f_x=0.5$ and 3.0 N/kg the boundary layers are significantly thinner on the downstream (right-hand) surface than they are on the upstream side. They are especially thin near the groove opening. This reversed boundary layer development is caused by the reversed flow in the groove, i.e., groove vortex. At $f_x=3.0$ N/kg, a very thin boundary layer also forms on the upstream (left-hand) wall near the groove trough. At this forcing level, the groove vortex is sufficiently strong to impinge fluid directly against that surface.

Figure 6 shows numerical and experimental center point Nusselt number versus location. The numerical results are for $f_x=3.0$ and 12.5 N/kg, corresponding to time average Reynolds numbers of $\mathrm{Re}_a=849$ and 1630, respectively. The experimental results are for Re=800 and 1600 ([12]). While the simulations calculate heat transfer in the fully developed region of the channel, the measured results at Re=800 are in the developing region.

The experimental and numerical data are in good quantitative agreement on the upstream portion of the groove. Both sets of data exhibit very similar plateaus near $x/b=0.35$ due to impingement of the groove vortex. Both data sets indicate that the Nusselt number on the downstream surface is greater than that on the upstream side. At $\mathrm{Re}_a=1630$, however, the numerical results are significantly higher than the experimental data, especially near the lip of the groove ($x/b=1$). The experimental result plateaus at roughly $\mathrm{Nu}_c=27$ while the numerical results reach considerably higher values. This difference may be due to differences in the thermal boundary conditions since the simulations do not account for conjugate heat transfer in the grooved walls. Alternately, the numerical grid may be slightly underresolved for high Reynolds

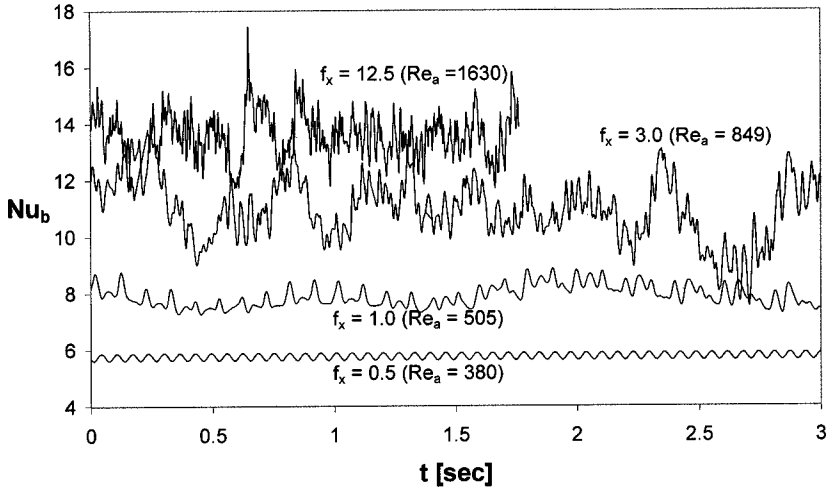

Fig. 7 Bulk Nusselt number versus time

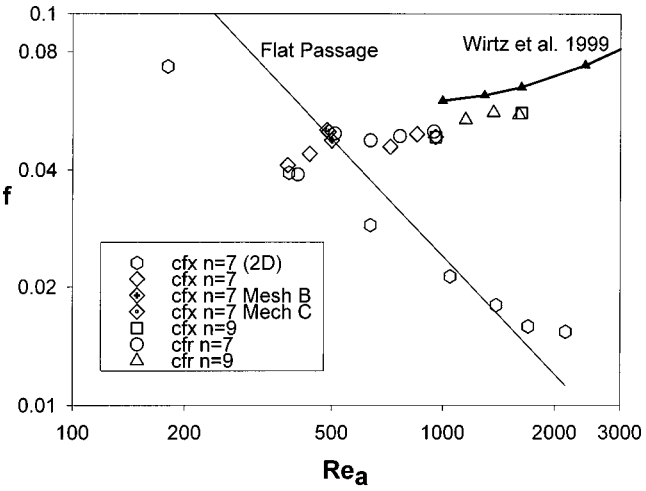

Fig. 8 Fanning friction factor versus Reynolds number

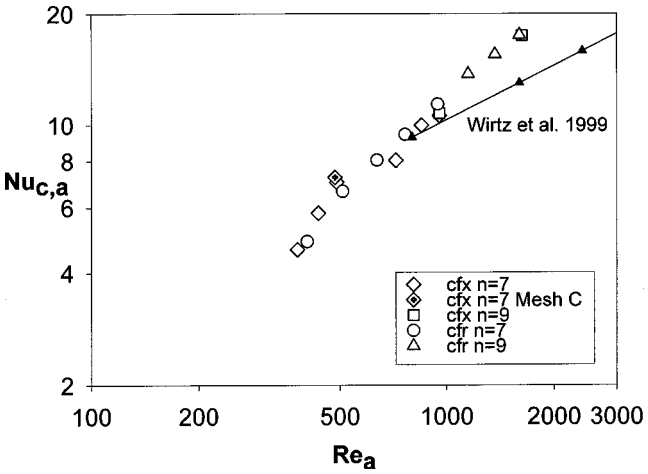

Fig. 10 Center point Nusselt number versus Reynolds number

numbers simulations (as discussed in the next section), or the experimental holographic technique may have been unable to accurately measure very large heat fluxes.

Figure 7 shows the time-dependent bulk Nusselt number, averaged over the entire computational domain, for the same four forcing levels as Fig. 4. For $f_x = 0.5$ N/kg the two-dimensional wave motion exhibited in Fig. 2 causes regular Nusselt number variations with the same period as the Reynolds number oscillations. Furthermore, examination of the data shows that the time dependent Nusselt number from two-and three-dimensional simulation is the same. Generally speaking, the time scales of the Nusselt number variations exhibited in Fig. 7 are similar to those of the Reynolds number in Fig. 4. However, the amplitude of the Nusselt number unsteadiness is greater than that of the Reynolds number.

Transport Quantities. Figures 8–10 show time average transport quantities versus Reynolds numbers from both constant f_x (cfx) and constant flow rate (cfr) simulations. Fanning friction factor, bulk Nusselt number and center point Nusselt number are shown in Figs. 8, 9, and 10, respectively. All of these quantities are averaged over time and the computational domain. Experimental results from [12] for friction factor and center point heat transfer are included in Figs. 8 and 10. The 99 percent confidence intervals for the measured Reynolds numbers, friction factors and Nusselt numbers are less than 7.1 percent, 15 percent, and 15 percent of the respective values.

All two-dimensional and low Reynolds number ($Re_a < 1000$) three-dimensional simulations employ seventh-order spectral elements ($N = 7$). Simulations for the more refined and wider meshes (B and C, respectively) at $Re_a \approx 500$ also use $N = 7$. Higher Reynolds number simulations use ninth-order elements ($N = 9$).

At $Re_a \approx 500$, where the size of the dominant three-dimensional flow structures are fairly close to the dimensions of the computational domain, the results are independent of the domain width (mesh C) and the number of z-levels of the grid (mesh B). At $Re \approx 950$, where the flow field is highly three-dimensional, the results are effectively independent of simulation order ($N = 7$ or 9). The constant f_x (cfx) and constant flow rate (cfr) results in Figs. 8–10 are also nearly the same, except that the cfr correlations are slightly smoother than the cfx results. This indicates that flow rate unsteadiness has a much smaller effect on heat transfer at supercritical Reynolds number than it does at subcritical values. These results indicate that the numerical data are grid and forcing function independent for $Re_a \lesssim 950$. However, the highest Reynolds number results must be regarded as somewhat speculative since no spatial resolution study was performed for $Re_a > 1000$. On the other hand, the numerical results are in fair agreement with the available experimental data.

The two and three-dimensional friction factor results shown in Fig. 8 are essentially identical for Reynolds numbers at and below $Re_a = 380$ but they diverge at higher flow rates. A solid line shows the fully developed Fanning factor for a laminar flat passage with the same minimum wall to wall spacing as the grooved channel. The two-dimensional simulations predict that the friction factor decreases with Reynolds number, similar to unmixed flow in a laminar flat passage. The three-dimensional simulations on the other hand predict that the friction factor rises from $Re_a = 380$ to 490, drops by roughly ten percent from $Re_a = 490$ to 720, and then gently increases from $Re = 720$ to 1600.

At low Reynolds numbers, the grooved channel friction factors are *below* the flat passage values. We note that these passages have the same *minimum* wall to wall spacing. At low Reynolds numbers, the grooved passage flow field is steady and the grooves essentially act to relax the no-slip boundary conditions. The onset of unsteadiness at $Re_a = 380$ causes its friction factor to increase beyond that of the flat passage. The experimental and numerical friction factor data overlap in a fairly narrow Reynolds number range, $1000 < Re_a < 1600$. Within this range the numerically predicted values are roughly 20 percent below the measured values.

The bulk Nusselt numbers from the two and three-dimensional simulations shown in Fig. 9 are identical for Reynolds numbers

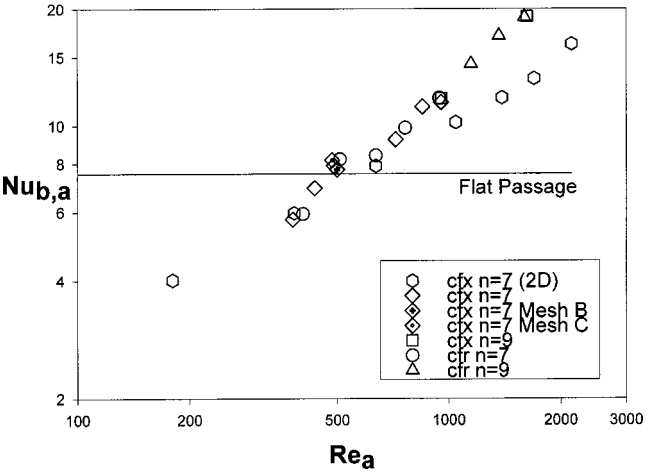

Fig. 9 Bulk Nusselt number versus Reynolds number

less than $Re_a=380$, similar to the friction factor behavior. At higher Reynolds numbers three-dimensional mixing causes the heat transfer to be greater than the level predicted from two-dimensional simulations. This divergence is much smaller for the bulk Nusselt number than it is for friction factor. At $Re_a=1000$, the two-dimensional friction factor results are smaller than the three-dimensional result by a factor of more than two, while the heat transfer results are only 20 percent low. At low Reynolds numbers, the grooved channel Nusselt number is smaller than the flat passage value (shown using a solid line) due to the thermal resistance of the slow moving fluid in the grooves. The onset of unsteady mixing causes the grooved channel heat transfer to increase beyond the flat passage value for Reynolds numbers above $Re_a=500$.

Figure 10 compares the center point Nusselt numbers from the current three-dimensional simulation with experimental data from [12]. As mentioned earlier, the experiments use the temperature at the center of the domain to characterize the fluid temperature instead of the bulk value. Our calculations show that the center point Nusselt number is 20 percent below the bulk value at $Re_a=435$, but the two values are within ten percent at $Re_a=849$, where the flow is well mixed. In the range $800<Re<1000$ the numerically predicted Nusselt number is slightly above the experimental data. At higher Reynolds numbers, however, the slope of the numerical Nu_c versus Re dependence is significantly greater than the measured value. As mentioned in connection with Fig. 6, this difference may be traced to differences on the downstream groove lip.

Summary

Navier-Stokes simulations of three-dimensional flow and augmented convection in a fully developed, symmetrically grooved passage were performed using the spectral element technique. These simulations were performed over the Reynolds number range $180\leqslant Re\leqslant 1600$. Simulations were performed using both a constant body force and a constant flow rate condition to drive the flow. A method employing an exponentially decaying temperature scale was developed to calculate the fully developed heat transfer coefficient for constant temperature boundary conditions.

The evolution of the velocity and temperature fields as the Reynolds number is increased, from steady two-dimensional flow to coherent traveling wave structures to three-dimensional mixing, has been documented. The simulations exhibited good quantitative agreement with the measured local Nusselt number profile at $Re_a=800$. However, at high Reynolds numbers the simulations predicted greater heat transfer levels than the experimental results on the downstream surface of the groove.

Two-dimensional simulations did not accurately predict the spatially and temporally averaged friction factor for $Re_a>400$, or the heat transfer for $Re_a>1000$. However, three-dimensional calculations predicted friction factor and heat transfer results that were within 20 percent of measured values in the range $800<Re_a<1600$. The results from constant body force and constant flow rate simulations were nearly identical, indicating that flow rate unsteadiness has little effect on transport at supercritical Reynolds numbers.

Acknowledgment

National Science Foundation Grant CTS-9501502 supported this work. The work of P. F. Fischer was supported by the Mathematical, Information, and Computational Sciences Division subprogram of the Office of Advanced Scientific Computing Research, U.S. Department of Energy, under Contract W-31-109-Eng-38. The California Institute of Technology provided time on the Intel Paragon under NSF Cooperative Agreement CCR-8809616.

Nomenclature

a = groove depth, Fig. 1
b = channel periodicity length, Fig. 1
c = decay constant
D_h = hydraulic diameter of minimum cross section, $2H$
f = Fanning friction factor, $(f_x D_h)/(2U_a^2)$
f_x = fluid body force per unit mass in the x-direction
H = minimum channel wall to wall spacing, Fig. 1
k = fluid thermal conductivity, 0.0263 W/m°C
K = number of spectral elements
$\hat{n}$ = wall normal unit vector
N = spectral element order
Nu_b = bulk Nusselt number based on projected area
Nu_c = center point Nusselt number
Pr = fluid molecular Prandtl number, 0.70
Re = Reynolds number, UD_h/ν
Re_a = time-average Reynolds number, $U_a D_h/\nu$
t = time
T = temperature
T_b = bulk temperature
T_c = center point temperature
u, v, w = velocity components in the x, y, and z-directions
U = mean x-velocity at the minimum channel cross section
U_a = time-average U
V = volume
W = width of the computational domain, Fig. 1

Greek

α = thermal diffusivity, 2.63×10^{-5} m^2/s
ν = fluid kinematic viscosity, 1.84×10^{-5} m^2/s
θ = periodic temperature
ρ = fluid density, 1.006 kg/m^3
τ = period of local time variations
Ω = computational domain

References

[1] Webb, R. L., 1994, *Principles of Enhanced Heat Transfer*, John Wiley and Sons, New York.
[2] Ghaddar, N. K., Korczak, K., Mikic, B. B., and Patera, A. T., 1986, ''Numerical Investigation of Incompressible Flow in Grooved Channels. Part 1: Stability and Self-Sustained Oscillations,'' J. Fluid Mech., **168**, pp. 541–567.
[3] Greiner, M., 1991, ''An Experimental Investigation of Resonant Heat Transfer Enhancement in Grooved Channels,'' Int. J. Heat Mass Transf., **24**, pp. 1383–1391.
[4] Roberts, E. P. L., 1994, ''A Numerical and Experimental Study of Transition Processes in an Obstructed Channel Flow,'' J. Fluid Mech., **260**, pp. 185–209.
[5] Kozlu, H., Mikic, B. B., and Patera, A. T., 1988, ''Minimum-Dissipation Heat Removal by Scale-Matched Flow Destabilization,'' Int. J. Heat Mass Transf., **31**, pp. 2023–2032.
[6] Karniadakis, G. E., Mikic, B. B., and Patera, A. T., 1988, ''Minimum-Dissipation Transport Enhancement by Flow Destabilization: Reynolds Analogy Revisited,'' J. Fluid Mech., **192**, pp. 365–391.
[7] Amon, C. H., Majumdar, D., Herman, C. V., Mayinger, F., Mikic, B. B., and Sekulic, D. P., 1992, ''Experimental and Numerical Investigation of Oscillatory Flow and Thermal Phenomena in Communicating Channels,'' Int. J. Heat Mass Transf., **35**, pp. 3115–3129.
[8] Greiner, M., Chen, R.-F., and Wirtz, R. A., 1989, ''Heat Transfer Augmentation Through Wall-Shaped-Induced Flow Destabilization,'' ASME J. Heat Transfer, **112**, pp. 336–341.
[9] Greiner, M., Chen, R.-F., and Wirtz, R. A., 1991, ''Enhanced Heat Transfer/Pressure Drop Measured From a Flat Surface in a Grooved Channel,'' ASME J. Heat Transfer, **113**, pp. 498–500.
[10] Greiner, M., Spencer, G., and Fischer, P. F., 1998, ''Direct Numerical Simulation of Three-Dimensional Flow and Augmented Heat Transfer in a Grooved Channel,'' ASME J. Heat Transfer, **120**, pp. 717–723.
[11] Ghaddar, N. K., Magen, M., Mikic, B. B., and Patera, A. T., 1986, ''Numerical Investigation of Incompressible Flow in Grooved Channels. Part 2: Resonance and Oscillatory Heat Transfer Enhancement,'' J. Fluid Mech., **168**, pp. 541–567.
[12] Wirtz, R. A., Huang, F., and Greiner, M., 1999, ''Correlation of Fully Developed Heat Transfer and Pressure Drop in a Symmetrically Grooved Channel,'' ASME J. Heat Transfer, **121**, pp. 236–239.
[13] Patera, A. T., 1984, ''A Spectral Element Method for Fluid Dynamics; Laminar Flow in a Channel Expansion,'' J. Comput. Phys., **54**, pp. 468–488.
[14] Maday, Y., and Patera, A. T., 1989, ''Spectral Element Methods for the

Navier-Stokes Equations,'' *State of the Art Surveys on Computational Mechanics*, A. K. Noor and J. T. Oden, eds, ASME, New York, pp. 71–143.
[15] Orszag, S. A., and Kells, L. C., 1980, ''Transition to Turbulence in Plane Poiseuille Flow and Plane Couette Flow,'' J. Fluid Mech., **96**, pp. 159–205.
[16] Fischer, P. F., and Patera, A. T., 1992, ''Parallel Spectral Element Solutions of Eddy-Promoter Channel Flow,'' *Proceedings of the European Research Community on Flow Turbulence and Computation Workshop*, Lausanne, Switzerland, Cambridge University Press, Cambridge, UK, pp. 246–256.
[17] Patankar, S. V., Liu, C. H., and Sparrow, E. M., 1977, ''Fully Developed Flow and Heat Transfer in Ducts Having Streamwise Periodic Variations of Cross-Sectional Area,'' ASME J. Heat Transfer, **99**, pp. 180–186.
[18] Kays, W. M., and Crawford, M. E., 1993, *Convection Heat and Mass Transfer*, 3rd Ed., McGraw-Hill, New York.
[19] Fischer, P. F., and Patera, A. T., 1991, ''Parallel Spectral Element Solutions of the Stokes Problem,'' J. Comput. Phys., **92**, pp. 380–421.
[20] Fischer, P. F., and Ronquist, E. M., 1994, ''Spectral Element Methods for Large Scale Parallel Navier-Stokes Calculations,'' Comp. Meth. Mech. Eng., pp. 69–76.